COMPARISON BETWEEN ANALYTICAL AND OPTIMAL CONTROL TECHNIQUES IN THE DIFFERENTIAL DRAG BASED RENDEZ-VOUS

Lamberto Dell'Elce, **Gaëtan Kerschen**
University of Liège, Space Structures & Systems Laboratory,
1,Chemin des Chevreuils, Liège, Belgium, Tel.: +32 4366 9449,
lamberto.dellelce@ulg.ac.be

Abstract: *The focus of this study is on differential drag for propellantless satellite rendez-vous. This technique is particularly attractive for low-Earth-orbit small satellites for which stringent weight constraints apply. Most existing contributions are based on bang-bang strategies, which may be difficult to implement in practice. This is why the present paper proposes a novel strategy integrating pseudospectral optimal control for maneuver planning and model predictive control for dealing with uncertainties and unmodeled dynamics. One important advantage of this methodology is that it can naturally account for attitude dynamics and constraints, which, in turn, paves the way for the practical realization of differential drag-based rendez-vous. A realistic scenario involving two nanosatellites of the QB50 constellation is considered to illustrate and validate the proposed developments. In addition, a comparison of this numerical technique with an existing analytic solution is carried out, and their respective pros and cons are discussed.*

Keywords: *Differential drag, optimal control, Radau pseudospectral transcription.*

1. Introduction

Optimization is a key factor in mission design, especially when dealing with formation flying, where severe size and weight constraints may strongly limit the performance of the propulsive system. Nowadays, propellantless techniques for formation flying, e.g., solar sail [1], geomagnetic [2], and Coulomb formation flying [3], are envisaged as possible solutions to either reduce or even remove the need for on-board propellant. This paper focuses on a propellantless technique based on the differential drag concept. By controlling the surface exposed to the residual atmosphere, it is possible to change the magnitude of the atmospheric drag and therefore to create a differential force, between one spacecraft (chaser) and either another spacecraft or a desired target point. This force can be exploited to control the relative position between the chaser and the target in the orbital plane, which enhances the maneuverability of small satellites in low-Earth orbits (LEO). The ORBCOMM constellation is the first application of the differential drag technique in space, though it is only limited to station-keeping [4]. The mission JC2sat, planned by JAXA and CSA, also proves the overall interest in the technique [5].

The exploitation of differential drag for LEO spacecraft was first introduced by Leonard [6], who developed a strategy for controlling the cross section with the aim of achieving a rendez-vous within the linear dynamics equations of Hill-Clohessy-Wiltshire. The idea of decomposing the relative movement into a mean and a harmonic component was also proposed in order to gain deep insight in the physical behavior of the problem. However, the methodology relied upon several restrictive assumptions, including circular

orbits, Earth approximated as a point mass, and a uniform atmosphere. Motivated by the desire to consider more representative scenarios, Bevilacqua *et al.* included the secular perturbations of the Earth's oblateness in Lambert's method [7]. They also proposed a hybrid approach combining differential drag and continuous low-thrust [8] aimed at enhancing out-of-plane controllability. Finally, a novel approach for bang-bang control based on an adaptive Lyapunov control strategy was developed to account for nonlinear orbital dynamics [9]. Kumar and Ng implemented the solution in a high-precision propagator [10], and they highlighted the importance of accurate mean states estimation in order to prevent the solution from drastic deterioration. Lambert *et al.* [11] overcame this issue by exploiting a conversion from osculating to mean orbital elements of both the target and the chaser. Though Kumar and Ng [12] proposed a continuous control approach, most of the literature on differential drag considers the bang-bang control of the cross section.

When relative ballistic coefficient control is achieved through attitude actuators, the assumption of bang-bang control is restrictive, especially for small satellites with limited power available. This is why we proposed in [13] a non-bang-bang optimal control algorithm that was able to account for attitude constraints. However, the resulting strategy showed a large computational cost, which complicates its implementation aboard a satellite. The present study is the extension of [13] and has a twofold objective. First, a novel optimal control approach for differential drag-based rendez-vous is proposed. The method involves a maneuver planner based on a Radau pseudospectral transcription and on-line corrections relying on nonlinear model predictive control (MPC). Second, some of the practical challenges that are intimately related to the exploitation of the differential drag in a realistic scenario are addressed. A detailed comparison between an existing analytical technique and the proposed algorithm is then carried out.

The paper is organized as follows. Section 2 describes the different building blocks of the proposed optimal control strategy. Section 3 reviews the existing analytical method [7]. The two methods are compared in Section 4 considering two nanosatellites of the QB50 constellation. The comparison focuses on two main aspects, namely the values of the merit functions and the flexibility with respect to the introduction of attitude constraints. All the results obtained in this section are based upon high-fidelity orbital propagations. Finally, section 5 summarizes the main results of this study and discusses the future directions of our work.

2. Optimal control

Consider the rendez-vous problem schematized in Fig. **1**. We suppose that the target has a stable attitude, while the rotation about the orbital plane of the chaser is controlled via a single reaction wheel with inertia I_w, maximum torque T_w, angular velocity with respect to the spacecraft ω_w, and operating range $[\omega_{w,l}, \omega_{w,u}]$. Unlike the other methods proposed in the literature, the controlled variable, u, is not the differential drag, but the torque provided to the reaction wheel.

The proposed optimal control algorithm consists of three main modules: 1) the maneuver planner computes the off-line global maneuver, 2) a MPC algorithm accounts for on-line corrections, 3) the drag estimator evaluates the ballistic coefficient by fitting the observed mean semi-major axis. The high-level control strategy is illustrated in Fig. **2**.

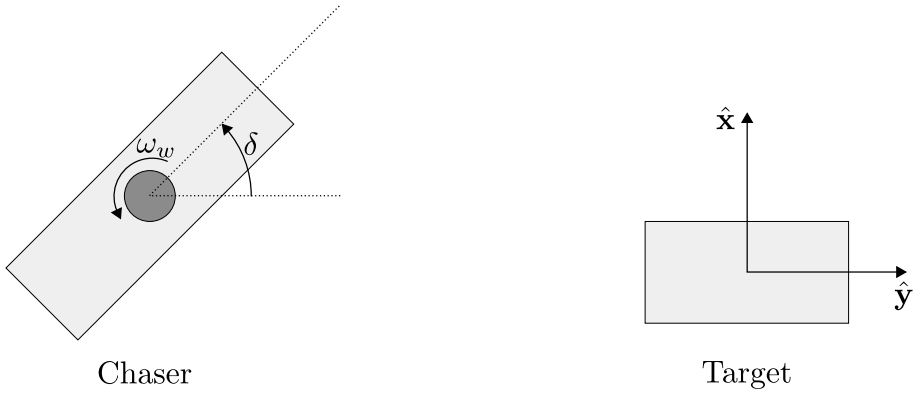

Figure 1: **Attitude dynamics notation. The target is supposed to fly with the long axis aligned to the orbital velocity direction.**

The drag estimator and the maneuver planner are activated few times within the maneuver. In this work, we only execute these two modules once at the beginning of the maneuver.

The optimal control problem exploits dynamics equations in the decomposed curvilinear relative states. In particular, denoting $\tilde{x}$ and $\tilde{y}$ as the radial and in-track position of the chaser with respect to the target, the corresponding decomposition involves the identification of a mean, $(\tilde{x}_m, \tilde{y}_m)$, and an oscillatory component, $(\tilde{x}_o, \tilde{y}_o)$, such that $\tilde{x}_m + \tilde{x}_o = \tilde{x}$ and $\tilde{y}_m + \tilde{y}_o = \tilde{y}$. The definition of these variables is detailed in the Appendix A.

2.1. Maneuver planner

The maneuver planner computes the off-line optimal control strategy for the global rendez-vous maneuver. The optimal control problem is solved with an *hp*-adaptive Radau pseudospectral transcription [14] using the software GPOPS. The trade-off between computational cost and accuracy is the key driver of the synthesis of the planner. The problem

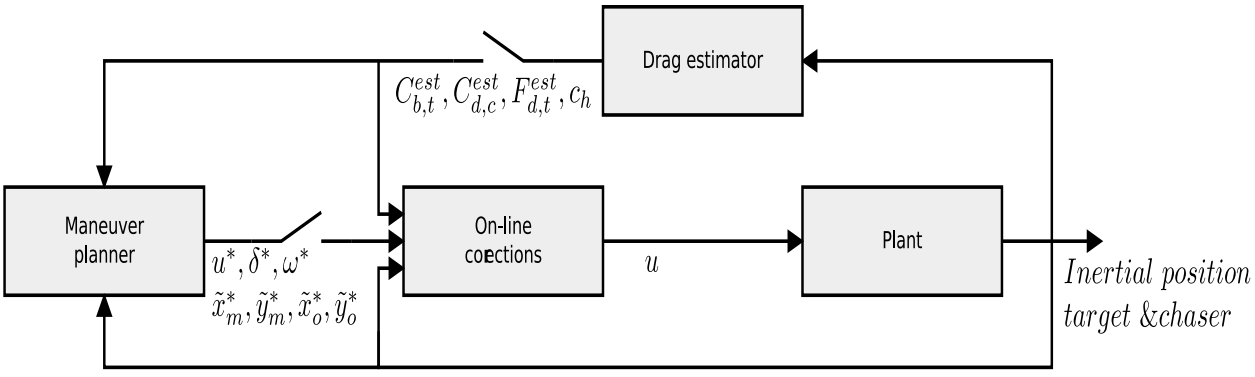

Figure 2: **Top level optimal control strategy.**

is posed in Bolza form

$$u^*(t) = \arg\left[\min_{u(t)}\left(t_f + W\int_0^{t_f} u^2\right)\right] \quad subject\ to \tag{1}$$

$$\omega_w \in [\omega_{w,l}, \omega_{w,u}], \quad |u| \le T_w \quad \forall\, t \in [0, t_f] \tag{2}$$

$$\begin{aligned} \tilde{x}_m(0) = \tilde{x}_{m,0},\ \tilde{x}_o(0) = \tilde{x}_{o,0}, \quad \delta(0) = \delta_0,\ \dot{\delta}(0) = 0 \\ \tilde{y}_m(0) = \tilde{y}_{m,0},\ \tilde{y}_o(0) = \tilde{y}_{o,0}, \qquad \omega_w(0) = \omega_{w,0} \end{aligned} \tag{3}$$

$$\tilde{x}_m(t_f) = \tilde{y}_m(t_f) = \tilde{x}_o(t_f) = \tilde{y}_o(t_f) = 0 \tag{4}$$

$$\begin{cases} \dot{\tilde{x}}_m &= \frac{2c}{(2-c^2)\omega}\,\Delta F_d\,(\delta, \tilde{x}_m + \tilde{x}_o, t) \\ \dot{\tilde{y}}_m &= \frac{\left(2-5c^2\right)\omega}{2c}\,\tilde{x}_m \\ \dot{\tilde{x}}_o &= \frac{\left(2-c^2\right)\omega}{2c}\,\tilde{y}_o - \frac{2c}{(2-c^2)\omega}\,\Delta F_d\,(\delta, \tilde{x}_m + \tilde{x}_o, t) \\ \dot{\tilde{y}}_o &= -2\omega c\,\tilde{x}_o \\ \ddot{\delta} &= I_{sat}^{-1}\,(M_{ext} - u) \\ \dot{\omega}_w &= \left(I_{sat}^{-1} + I_w^{-1}\right) u - I_{sat}^{-1}\,M_{ext} \end{cases} \quad \forall\, t \in [0, t_f] \tag{5}$$

where W, M_{ext}, I_{sat}, and ΔF_d are a user-supplied weight, the external aerodynamic torque on the chaser, the rotational inertia of the chaser without the reaction wheel, and the estimated differential drag, as discussed in Section 2.3. The initial guess for the NLP is provided by the analytical solution described in Section 3, and propagated in linearized dynamics.

The performance index (Eq. 1) wants to minimize both the maneuvering time, t_f, and the total action of control, which is intimately related to the power consumption of the attitude control system. The weight W is selected such that the control term of the performance index is dominant. In fact, the maneuvering time exhibits low sensitivity with respect to W, since the optimal solution is attracted by the initial guess. On the contrary, a low W results in excessive control action of several orders of magnitude. Physical constraints include the maximum available torque and the operating range of the wheel, and they are naturally introduced through the side constraints of Eq. 2.

Equations 3 and 4 express the initial and rendez-vous conditions, respectively.

The differential equations 5 govern the relative movement and attitude dynamics. Since the direct transcription enforces dynamics equations as equality constraints in a nonlinear programming (NLP) optimization problem, the proper choice of the differential equations is the core of the trade-off between accuracy and computational efficiency:

- the planner is required to be consistent with the real dynamics. Consistency implies that *all* the dominant effects are modeled. This includes short period and altitude-dependent variations of the drag. When propagating the open loop control, we observed that neglecting short period variations reflects in inconsistent predictions of the oscillatory movement, while neglecting altitude dependency results in larger in-track errors at the end of the maneuver.

- targeting computational efficiency, we want that *only* the dominant effects are modeled in the planner. This excludes all the orbital perturbations but the drag and secular J_2 effects. Assuming distances up to few hundreds kilometers, the phase

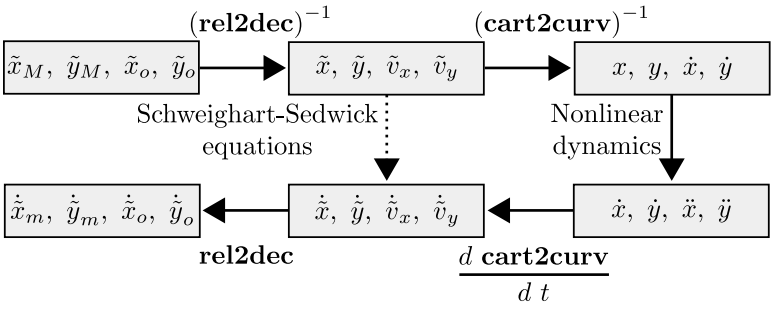

Figure 3: **Schematic representation of the computation of the right hand term of the differential equation. Computational efficiency is achieved using the linearized equations of motion. The nomenclature of the operators is detailed in appendix A.**

delay between the drag acting on the two satellites can also be safely neglected. Furthermore, only an averaged linear dependency of the differential drag on the altitude gap is considered through the coefficient c_h, which is provided by the drag estimator (see Section 2.3). So, assuming that the drag of the chaser is proportional to the exposed cross-section, the differential drag is computed as

$$\Delta F_d\left(\delta, \tilde{x}, t\right) = \left|F_{d,t}^{est}\left(t\right)\right| \left[1 - \frac{C_{d,c}^{est}\left(S_1|\cos\delta| + S_2|\sin\delta|\right)}{C_{b,t}^{est}\ m_c}\left(1 + c_h\tilde{x}\right)\right] \tag{6}$$

where, considering Fig. **1**, S_1 and S_2 are the surfaces of the small and large faces of the chaser, respectively, and m_c its mass. $C_{b,t}^{est}$, $C_{d,c}^{est}$, c_h, and $F_{d,t}^{est}$ are outputs of the drag estimator discussed in Section 2.3. Further efficiency is achieved by expressing relative dynamics in terms of decomposed curvilinear variables, which are "smoother" and more decoupled than relative states. Finally, in our previous method [13], the right hand term of the differential equation directly accounted for nonlinear dynamics, as illustrated by the solid path in Fig. **3**. Considering linearized dynamics (dotted path) largely enhances computational efficiency with very limited accuracy loss.

We stress that the *only* input of the planner are the initial conditions and the outputs of the drag estimator.

The output of the planner are the reference control and states in function of time, namely u^*, $\tilde{x}_m^*$, $\tilde{y}_m^*$, $\tilde{x}_o^*$, $\tilde{y}_o^*$, δ^*, ω_w^*.

2.2. On-line corrections

On-line corrections are mandatory to account for non-modeled dynamics and uncertainties. A model predictive control algorithm is developed to this purpose.

At each evaluation, the on-line controller solves a problem analogous to the maneuver planner. The only differences are the boundary conditions, the fixed horizon, and the performance index.

Initial conditions are provided by the current states at the beginning of the evaluation at time t. MPC is based upon the receding horizon principle, so that the final time is not

dependent on event constraints like Eq. 4, but the horizon is fixed to $t + t_h$. The computed corrected control is then applied to the plant for a time $t_c \leq t_h$. We selected $t_h = 2t_c = 2t_{orb}$. This combination allows for an adequate averaging of short period variations that are the most critical to predict.

The performance index is aimed at minimizing the divergence from the reference path

$$\int_t^{t+t_h} \left[W_x \left(\tilde{x}_m + \tilde{x}_o - \tilde{x}^* \right)^2 + W_y \left(\tilde{y}_m + \tilde{y}_o - \tilde{y}^* \right)^2 + W_\delta \left(\delta - \delta^* \right)^2 \right] d\tau \tag{7}$$

A direct contribution of the controlled variable is not included, because its variation is dominated by the variations of δ. The proper selection of the coefficients is not trivial, and stability issues may arise. Large W_δ means high confidence in the reference path, but a less efficient tracking. We tested different setup with initial in-track distances ranging up to 150km. Setting coefficients such that the three contributions have the same order of magnitude resulted in a stable controller within this range. However, our future research will investigate a robust and automatic procedure for tuning the coefficients. Ideally, a large W_h is more suitable for the first phase of the maneuver.

In conclusion, our on-line controller is activated once per orbit, and it computes an open loop control with two-orbit horizon.

2.3. Drag estimator

This module is in charge of the estimation of the drag force on the two satellites. For this purpose, it requires that their accurate position is monitored for a waiting time t_{obs} of at least two orbits. The attitude has to be stable throughout this period.

The estimation is performed by minimizing the mean square error between observed and simulated mean semi-major axis. Simulated data are generated through high-precision propagation based on the Jacchia 71 atmospheric model. This evaluation is necessary for both the analytical and the optimal control strategy.

The outputs of the drag estimator are the drag and ballistic coefficient of chaser and target, $C_{d,c}^{est}$ and $C_{b,t}^{est}$, respectively, the estimated time history of the drag of the target, $F_{d,t}^{est}$, and the altitude correction factor

$$c_h = \frac{1}{t_{obs}} \int_0^{t_{obs}} \frac{1}{\rho^{est}(\tau)} \left. \frac{\partial \rho^{est}}{\partial h} \right|_\tau d\tau \tag{8}$$

ρ^{est} and h being the estimated density and the local geodetic altitude, respectively.

3. Analytical technique

Most of the analytical methods in literature share common features [6, 7, 11]. In particular, these controllers are based on the current position in the curvilinear decomposed state diagrams, and on linearized dynamics, like the Schweighart-Sedwick equations [15]

$$\begin{aligned} \ddot{x} &= 2\omega c\, \dot{y} + \left(5c^2 - 2\right) \omega^2\, x \\ \ddot{y} &= -2\omega c\, \dot{x} + \Delta F_d \end{aligned} \tag{9}$$

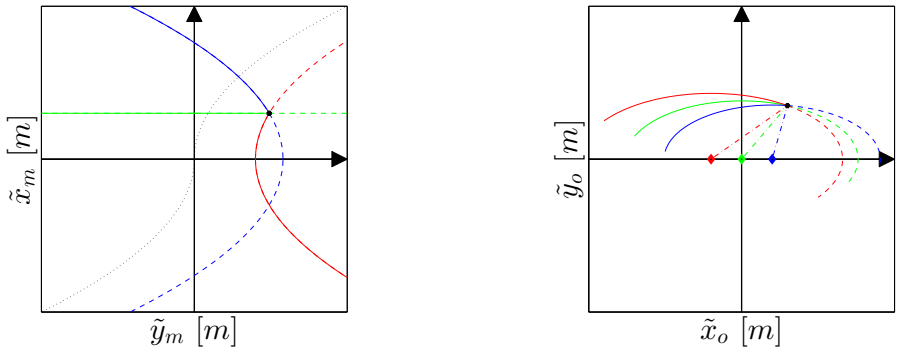

(a) Mean component. (b) Oscillatory component.

Figure 4: **Linear dynamics of the decomposed states. The chaser is initially located in the black point. The movement evolves in the direction of the solid lines. The blue and red curves indicate positive and negative differential drag, respectively, while green indicates the coasting trajectories. The black dotted line represents the switching curve.**

that assume a circular reference orbit, secular-only perturbations of the Earth oblateness, and differential drag, ΔF_d, aligned with $\hat{\mathbf{y}}$. Substituting rectangular with curvilinear coordinates in Eq. 9 strongly improves the accuracy of the solution for large range maneuvers.

By further assuming uniform atmospheric density, ρ, and neglecting short period variations in the orbital velocity, v, the differential drag is given by

$$\Delta F_d = -\frac{1}{2}\rho v^2 \left(C_{b,c} - C_{b,t}\right) \tag{10}$$

$C_{b,c}$ and $C_{b,t}$ being the chaser and target ballistic coefficients, respectively. If ΔF_d follows a bang-bang control strategy, the movement in the $(\tilde{x}_m, \tilde{y}_m)$ and $(\tilde{x}_o, \tilde{y}_o)$ diagrams evolves as a double integrator and a harmonic oscillator, respectively, as illustrated in Fig. **4**. Separate controllers are most often implemented for the two diagrams. The former aims at achieving the "switching curve" of Fig. **4** which drives mean states directly to the origin, the latter consists of tuning the sign of ΔF_d according to the sign of $\tilde{x}_o$. The concavity, of the parabolas in $(\tilde{x}_m, \tilde{y}_m)$ and the location of the centers of the ellipses in $(\tilde{x}_o, \tilde{y}_o)$ are proportional to the magnitude of the differential drag and to its inverse, respectively.

Strategies to conciliate the simultaneous control of the four states exist, but we observed a deterioration of the solution in this case that is mostly due to the important periodic variations of the drag throughout the orbit when considering high precision propagations.

Because of the several assumptions summarized in this section, the implementation of analytical controller in a realistic scenario is not straightforward and different aspects have to be adequately addressed. Firstly, the method requires the estimation of the differential drag, ΔF_d^{est}. This tasks is addressed by the same drag estimator discussed in Section 2.3. The second aspect concerns short period variations of the drag, which result in important time-dependent variations in the concavity of the switching curve. Substituting the estimated differential drag with its one-orbit-filtered counterpart,

$\Delta\bar{F}_d^{est}(t) = \int_{t-\frac{2\pi}{\omega}}^{t} \left|\Delta F_d^{(est)}(\tau)\right| d\tau$, fixes this issue, while still accounting for the long period trend of the drag. The resulting controller of the mean motion is quite robust, but once again oscillation reduction is more critical. For this reason, we consider the mean motion analytical controller only.

In this paper, we assume that differential drag is tuned through attitude control of the chaser, while $C_b^{(tgt)}$ is supposed to be constant. The only rotation about the off plane direction is modeled. These assumptions are in agreement with the test case detailed in Section 4. Considering the notation of Fig. **1**, the controlled variable is the angle of attack of the chaser, δ , which is such that

$$\begin{aligned} if\ \tilde{y}_m > \tilde{y}_s \quad or\ \left(\tilde{y}_m = \tilde{y}_s\ \&\ \dot{\tilde{y}}_m > 0\right) \quad &\Rightarrow \delta = 0\text{deg} \\ if\ \tilde{y}_m < \tilde{y}_s \quad or\ \left(\tilde{y}_m = \tilde{y}_s\ \&\ \dot{\tilde{y}}_m < 0\right) \quad &\Rightarrow \delta = 90\text{deg} \end{aligned}$$

where $\tilde{y}_s = \frac{3}{8}\omega^2 \left|\tilde{x}_m\right| \tilde{x}_m \Delta\bar{F}_d^{est^{-1}}$ is the in-track component of the switching curve [11]. A finer attitude modeling is not straightforward with analytical techniques. This aspect is further argued in Section 4.

4. Comparison

This section is devoted to the comparison of the two discussed techniques. The test case analyzed concerns two satellites of the QB50 constellation. In particular, the chaser is QARMAN, a triple-unit CubeSat developed by the Von Karman Institute, whose mission consists in the study of the atmospheric reentry process. The University of Liège is developing a payload aboard QARMAN devoted to the in-orbit validation of differential-drag-based maneuvers. The target can potentially be any other standard QB50 spacecraft, which are double-unit CubeSats, and which are constrained to fly with the long axis aligned to the orbital velocity.

The simulation parameters are listed in Table **1**. The simulations are run on a processor intel i5 at 1.7 GHz. Our orbital propagator includes gravitational perturbations up to order and degree 10, solar radiation pressure, third-body perturbations of sun and moon, and perturbations of the polar axis. The atmospheric model is NRLMSISE-00. On top of that, a 30% bias and short period stochastic variations are included to make the scenario more realistic. The realization of the stochastic process is performed according to the density variation model proposed by Zijlstra [16]. Figure **5** illustrates the power spectral density of the process. The figure also illustrates the estimated drag of the target, that is far from being highly accurate. We emphasize that the drag estimator exploits a different drag model, i.e., Jacchia 71, than the propagator. All these aspect want to make the scenario as realistic as possible. However, our propagator is not yet able to estimate the aerodynamic torque, which is neglected. Our future work will account for this.

The comparison is performed on two levels. On the one hand, figures of merit are compared. On the other hand, qualitative and functional aspects are analyzed to get insight in the origin of the very different performance of the methods.

Table **2** lists the performance indicators. As expected, computational cost is the main strength of the analytical method. Though the analytical controller is accessed with high

Table 1: **Simulation parameters.**

Mean elements of the target	semi-major axis	$6728 \cdot 10^3$ m
	eccentricity	0
	inclination	98 deg
	RAAN	90 deg
	argument of perigee	0 deg
	true anomaly	0 deg
	Julian date	2455287.5
Initial gap of the chaser	in-track	$50 \cdot 10^3$ m
	radial	100 m
Space weather	Daily solar flux	200 sfu
	81-day averaged flux	155 sfu
	geomagnetic index K_p	4
Target properties	ballistic coefficient	0.014 m^{2}kg^{-1}
Chaser properties	mass	4 kg
	dimensions	$0.3 \times 0.1 \times 0.1$ m^3
	drag coefficient	2.8
	inertia	$3.33 \cdot 10^{-2}$ kg m^2
Reaction wheel	maximum torque	$0.08 \cdot 10^{-3}$ N m
	dynamic operating range	$[-5500, 5500]$rpm
	inertia	$5.2 \cdot 10^{-6}$ kg m^2

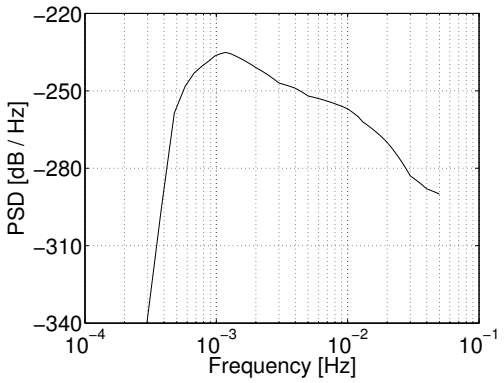

(a) Power spectral density of the short period variations [16].

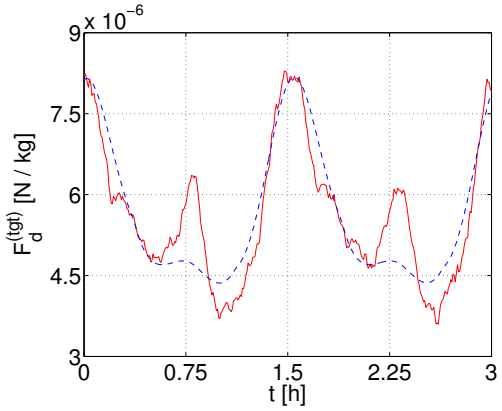

(b) Real (solid red) and estimated (dashed blue) drag of the target.

Figure 5: **Stochastic variations of the drag force.**

Table 2: **Comparison of the variables of interest.**

Variable	**Analytical**	**Optimal planner**	**Optimal on-line**
Computational cost	$2 \cdot 10^{-3}$ s/orbit	18.5 s	0.95 ± 0.63 s/orbit
Mean square control	$3.35 \cdot 10^{-6}$ N m	$9.99 \cdot 10^{-9}$ N m	$3.09 \cdot 10^{-8}$ N m
Maneuvering time	58 h 42 min	50 h 17 min	50 h 20 min

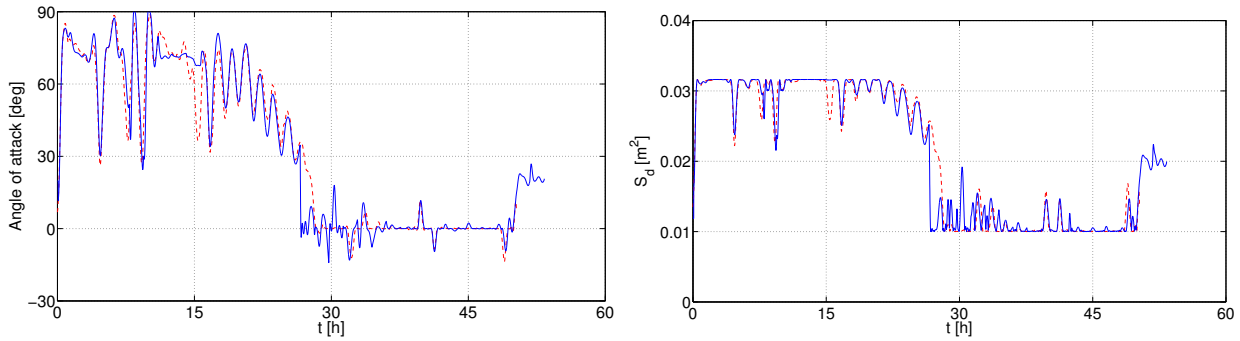

(a) (b)

Figure 6: **Angle of attack (a) and cross section of the chaser (b) in the optimal solution. Red dashed and solid blue are the planned and the on-line maneuver, respectively.**

rate, i.e., every 30s, the evaluation of the control is quasi instantaneous. On line corrections also need a reduced computational time but, while analytical evaluations are uniformly spread all around the orbit, the cost of the on-line controller is very localized and repeated at regular intervals. The maneuver planner requires the larger computational time, but we stress that it is run just once at the very beginning of the maneuver. When we tested the method with other initial conditions, we obtained a computational time ranging from 10 to 40s. Even if the microcontroller aboard the nanosatellite will be much less powerful, these numbers indicate that the practical implementation of the optimal control could be within reach.

The second figure of merit is the mean squared control action, $\sqrt{\frac{1}{t_f}\int_0^{t_f} u^2\, dt}$. The evaluation of this term requires additional modeling for the bang-bang solution. For this purpose, we converted each bang-bang switch with the fastest attitude maneuver. For a min-max switch it lasts in 53s. The whole analytical maneuver needs 10 switches. The inclusion of hysteretic bounds can reduce this number. However, assuming that only a single switch is necessary, it turns out that the mean squared control for a fifty-hour maneuver is $1.15 \cdot 10^{-6}$N m, which is still largely greater than the values obtained with the optimal solution. To understand the origin of this gain, consider the time history of the angle of attack for the optimal solution in Fig. **6**. No sharp variation is present throughout the whole maneuver. The controlled variable is also always applied largely below its admissible bounds. Furthermore, the fastest maneuver is also critical because wheel's saturation occurs after just 17s. On the contrary, the angular velocity of the wheel is always largely below the threshold in the optimal solution.

The third performance indicator is the maneuvering time. Also in this case, the performance of the analytic strategy is by far less good than that of optimal control, especially considering that the former drives to zero the mean states only. To better understand this result, the reader should consider Figures **7** and **8**. The analytical trajectory exhibits an important overshoot much more pronounced than the one in the optimal maneuver. This is due to the fact that the optimal on-line controller works by continuously attempting to track the reference path. For most of the maneuver, the planned angle of attack is not

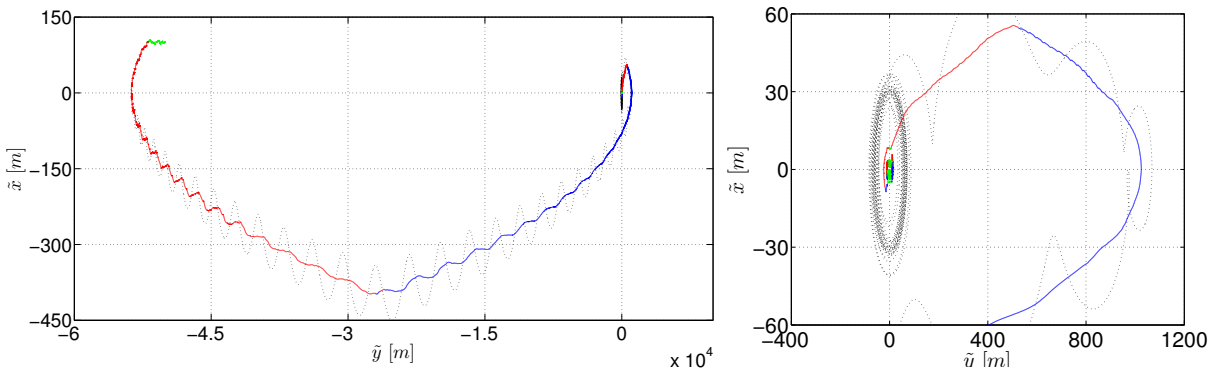

(a) Global trajectory. (b) Final phase.

Figure 7: **Analytical trajectory. The black dotted curve is the trajectory in relative curvilinear states. The colored curve is the only mean component. The color indicates the value of the angle of attack of the chaser. Red is 90deg, while blue is 0deg.**

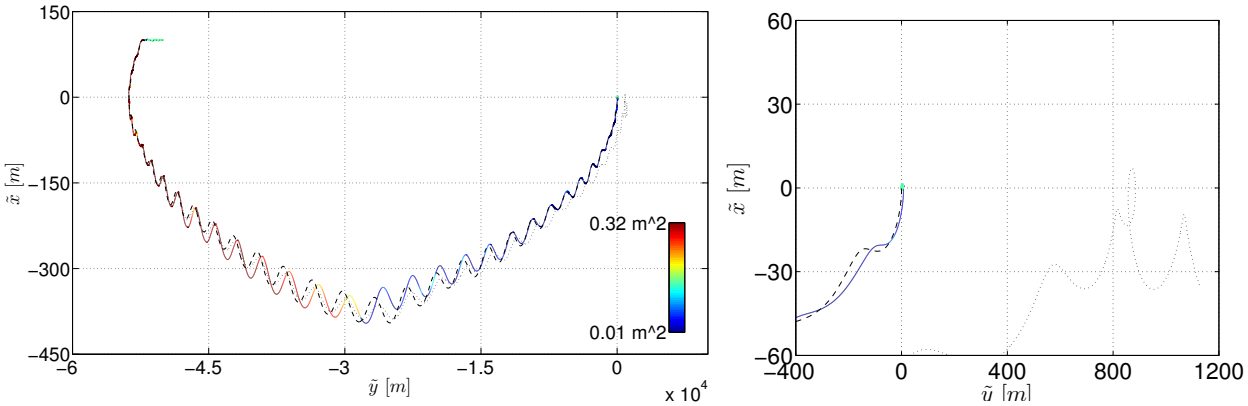

(a) Global trajectory. (b) Final phase.

Figure 8: **Optimal trajectory. The black dashed and dotted curves are the planned and the open-loop trajectories, respectively. The colored curve is the on-line trajectory. The color indicates the value of the cross section of the chaser. Dark blue is minimum cross-section, while red is maximum.**

such that differential drag is at its extreme (Fig. **6**), because the planner implicitly accounts for the reduction of the oscillatory component. This aspect leaves two-side margin of maneuverability to the on-line controller. On the other hand, bang-bang control strategy implies that the differential drag is always at its maximum or minimum level, so that there is not way back if the switching curve is missed because of either unmodeled dynamics or inadequate drag estimation. Figure **8** also allows to appreciate the consistency of the planner by comparing the reference and the open loop paths.

In conclusion the optimal controller exhibited larger flexibility in terms of capabilty to represent more complex dynamics and include arbitrary constraints. The optimization procedure also allows for extremely enhanced performance in terms of control action. An aspect that needs more investigation is the robustness of the MPC. For initial distances larger than 150km we experienced a divergence from the reference path in the final phase of the maneuver. Possible solutions that we will tailor involve the investigation of a robust procedure for the dynamic tuning of the objective function and the reset of the reference maneuver. In this case, analytical control may be implemented while waiting for the update of the reference path. Finally, we stress that for the two techniques, the *only* inputs for the overall algorithms are the accurate current positions of the two spacecraft.

5. Conclusions

The paper proposed a novel optimal control approach to the problem of the differential-drag-based rendez-vous. A detailed comparison with an analytical technique proved the superiority of the proposed algorithm under several aspects, namely the flexibility of the method and the optimization of performance indicators. On the other hand, analytical technique is still valuable for the reduced computational cost and to provide the optimal algorithm with an efficient initial guess.

We believe that this work paves the way for a practical realization of the differential drag for two reasons: 1) the proposed optimal control methodology is extremely promising for the optimization of the maneuver in terms of power resources and flexibility with respect to arbitrary constraints; 2) the overall methodology is developed by squeezing further the gap between real word and numerical implementation of the differential drag.

Our future work will follow three directions. The first is intended to achieve an automatic and robust tuning of the coefficients of the on-line controller. The possibility achieve its guaranteed stability will also be investigated. The second path will focus on the improvement of the mission scenario. High accuracy density model based on the Sentman theory will be integrated to the propagator, as well as detailed six-degree-of-freedom dynamics, and realistic state estimation. Finally, indirect transcription of the optimal control problem will be investigated, though our preliminary analysis suggests that the adequate estimation of the initial co-states is extremely challenging.

7. Acknowledgements

The author Lamberto Dell'Elce would like to acknowledge the Belgian National Fund for Scientific Research for its financial support (FRIA fellowship).

8. References

[1] Williams, T., Wang, Z.S., "Uses of solar radiation pressure for satellite formation flying," International Journal of Robust and Nonlinear Control, vol. 12, 2002, 163-183.

[2] Peck, M.A., Streetman, B., Saaj, C.M., Lappas, V., "Spacecraft Formation Flying using Lorentz Forces," Journal of the British Interplanetary Society, vol. 60, 2007, 263-267.

[3] King, L.B., Parker, G.G., Deshmukh, S., Chong, J.H., "Spacecraft Formation-flying using Inter-vehicle Coulomb Forces," Technical report, Michigan Technological University, 2002.

[4] Lewin, A.W., "Low-cost operation of the ORBCOMM constellation," Journal of Reducing Space Mission Cost, 1998, 105-117.

[5] Ng, A., Lambert, C., Hirako, K., Horiguchi, H., Nakamura, Y., "Japan Canada Joint Collaboration Satellites – Design of Intersatellite Separation Mechanism," International Astronautical Congress, Prague, 2010.

[6] Leonard, C.L., "Formationkeeping of spacecraft via differential drag," M.Sc. Thesis, Massachusetts Institute of Technology, Cambridge, 1986.

[7] Bevilacqua, R., Romano, M., "Rendezvous maneuvers of multiple spacecraft using differential drag under J_2 perturbation," Journal of Guidance, Control, and Dynamics, vol. 31, 2008, 1595-1607.

[8] Bevilacqua, R., Hall, J.S., Romano, M., "Multiple spacecraft assembly maneuvers by differential drag and low thrust engines," Celestial Mech. Dyn. Astron., 106, 2010 69–8.

[9] Pérez, D., Bevilacqua, R., "Differential drag spacecraft rendezvous using an adaptive Lyapunov control strategy," Acta Astronautica, vol. 83, 2013, 196-207.

[10] Kumar, B.S., Ng, A., "Bang-Bang Control approach to maneuver spacecraft in a formation with differential drag," AIAA Guidance, Navigation and Control Conference, AIAA, Honolulu, 2008.

[11] Lambert, C., Kumar, B.S., Hamel, J.F., Ng, A., "Implementation and performance of formation flying using differential drag," Acta Astronautica, vol. 71, 2012, 68-82.

[12] Kumar, B.S., Ng, A., "Time-optimal low-thrust formation maneuvering using a hybrid linear/nonlinear controller," Journal of Guidance, Control, and Dynamics, vol. 32, 2009, 343–347.

[13] Dell'Elce, L., Kerschen, G., "Orbital rendez-vous using differential drag in the QB50 constellation," AIAA-AAS Astrodynamics Specialists Conference, Minneapolis, 2012.

[14] Garg, D., Patterson, M.A., Hager, W. W., Rao, A.V., Benson, D.A., Huntington, G.T., "A Unified Framework for the Numerical Solution of Optimal Control Problems Using Pseudospectral Methods," Automatica, vol. 46, 2010, 1843-1851.

[15] Schweighart, S.A., Sedwick, R.J., "High-fidelity linearized J2 model for satellite formation flight," Journal of Guidance, Control, and Dynamics, Vol. 25, 1073–1080, 2002.

[16] Zijlstra, M., Theil, S., "Model for Short-term Atmospheric Density Variations," Earth Observation with CHAMP, Springer Berlin Heidelberg, 2005.

[17] Gim, D.W., Alfriend, K.T., "The State Transition Matrix of Relative Motion for the Perturbed Non- Circular Reference Orbit," AAS/AIAA Space Flight Mechanics Meeting, Santa Barbara, 2001.

[18] Schaub, H., "Incorporating the secular drifts into the orbit element difference description of relative orbits," AAS/AIAA Space Flight Mechanics Meeting, Ponce, 2003.

Appendix A. Variable transformations

This annex details the change of variables discussed in the paper.

osc2mean: this transformation consists in: (1) mapping the osculating Earth centered inertial (ECI) coordinates into classical keplerian elements, (2) converting osculating to mean elements [17], (3) recovering mean cartesian position from the mean elements.

abs2rel: absolute coordinates are converted into relative states in the Hill frame, which is centered in the target, with $\mathbf{e}_y$ axis aligned to the orbital velocity, $\mathbf{e}_z$ axis orthogonal to the orbital plane, and $\mathbf{e}_x = \mathbf{e}_z \times \mathbf{e}_y$ (Fig. **9**). In this paper we focus on the only in-plane components, that we refer to as x and y.

cart2curv: curvilinear coordinates are mandatory for middle and long range maneuvers. Mapping relative to curvilinear coordinates is achieved through the transformation

$$\begin{aligned} \tilde{x} &= \sqrt{(r_t + x)^2 + y^2} - r_t & \tilde{v}_x &= \dot{x}\cos\theta - \dot{y}\sin\theta \\ \tilde{y} &= r_{tgt}\,\theta & \tilde{v}_y &= \dot{x}\sin\theta + \dot{y}\cos\theta \end{aligned} \tag{11}$$

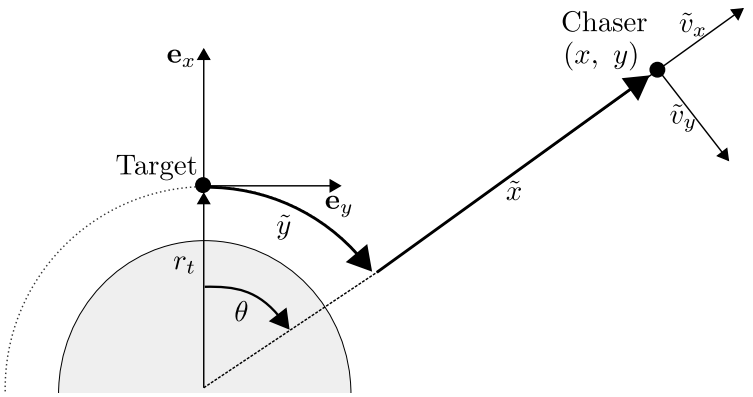

Figure 9: **Relative and curvilinear coordinates.**

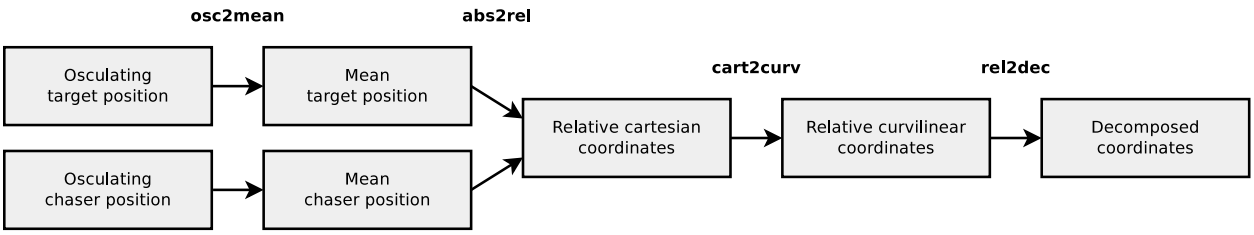

Figure 10: **Curvilinear relative state estimation from osculating orbital elements.**

where r_t is the actual mean radius of the target's orbit, and $\theta = \tan^{-1}\frac{y}{r_t+x}$. This transformation is illustrated in Fig. **9**.

rel2dec: relative states are decomposed into a mean and an oscillatory component, $(\tilde{x}_m, \tilde{y}_m)$ and $(\tilde{x}_o, \tilde{y}_o)$, respectively. Schweighart and Sedwick proposed a decomposition that accounts for the secular variations of the J_2 perturbation [15]. Though this transformation is rigorous for circular orbits, small distances and Hill coordinates, it is also valuable for curvilinear variables [18], so that it holds

$$\begin{aligned} \tilde{x}_m &= \frac{4c^2}{2-c^2}\tilde{x} + \frac{2c}{(2-c^2)\,\omega}\tilde{v}_y \qquad & \tilde{x}_o &= \tilde{x} - \tilde{x}_m \\ \tilde{y}_m &= \tilde{y} - \frac{2c}{(2-c^2)\,\omega}\tilde{v}_x \qquad & \tilde{y}_o &= \tilde{y} - \tilde{y}_m \end{aligned} \tag{12}$$

where $c = \sqrt{1 + \frac{3}{8}\frac{J_2}{r_t^2}\frac{R_e^2}{}(1+3\cos 2i_t)}$ is the Schweighart–Sedwick coefficient, while ω, R_e, and i_t are the orbital pulsation, the Earth radius, and the inclination of the reference orbit of the target, respectively.

Figure **10** illustrates the chain of transformations that drives to the estimation of the decomposed curvilinear states.